Materials Advances

ROYAL SOCIETY OF CHEMISTRY

REVIEW

View Article Online
View Journal | View Issue

Cite this: *Mater. Adv.*, 2024, 5, 6796

Degenerately doped metal oxide nanocrystals for infrared light harvesting: insight into their plasmonic properties and future perspectives

Mandeep Singh, [a] Francesco Scotognella*[b] and Giuseppe Maria Paternò *[a]

The tuneability of the localized surface plasmon resonance (LSPR) of degenerately doped metal oxide (MOX) nanocrystals (NCs) over a wide range of the infrared (IR) region by controlling NC size and doping content offers a unique opportunity to develop a future generation of optoelectronic and photonic devices like IR photodetectors and sensors. The central aim of this review article is to highlight the distinctive and remarkable plasmonic properties of degenerately or heavily doped MOX nanocrystals by reviewing the comprehensive literature reported so far. In particular, the literature of each MOX NC, *i.e.* ZnO, CdO, In_2O_3, and WO_3 doped with different dopants, is discussed separately. In addition to discussion of the most commonly used colloidal synthesis approaches, the ultrafast dynamics of charge carriers in NCs and the extraction of LSPR-assisted hot-carriers are also discussed in detail. Finally, future prospective applications of MOX NCs in IR photodetectors and photovoltaic (PV) self-powered chemical sensors are also presented.

Received 24th April 2024,
Accepted 30th July 2024

DOI: 10.1039/d4ma00426d

rsc.li/materials-advances

Introduction

The confinement of light at the nanoscale level *via* LSPR offers unique light–matter interactions[1,2] and proves to be highly efficient as it offers a unique pathway to enhancing the performance of many modern electronic devices, such as solar cells, gas sensors, biosensors, and light emitting diodes.[3–8] For a long time, LSPR was assumed to be a special property that was only associated with noble metal nanoparticles like Au or Ag.[1] However, beside their remarkable properties, LSPR in noble metals is a high-cost pathway and it does not offer tuneability due to the high and fixed density of charge carriers in metals ($\sim 10^{23}$ cm^{-3}).[1]

The discovery of LSPR in degenerately doped MOX nanocrystals (NCs) such as aluminium-doped ZnO (AZO), tin-doped indium oxide (ITO), or WO_3, opens up a new possibility for developing a future generation of optoelectronic and photonic devices.[1,9,10] LSPR in doped semiconductors holds an advantage over metal nanoparticles because their LSPR can be tuned from the THz to the NIR region by controlling the doping level and NC size, as shown in Fig. 1.[11] This is a two-dimensional Drude–Lorentz plot of NC size *vs.* LSPR frequency. As can be seen from Fig. 1, for degenerately doped semiconductors, by controlling the doping concentration between 10^{19} and 10^{21} cm^{-3}, the LSPR can be tuned from the far infrared (FIR) to the near-infrared (NIR) region. The wide range of tuneability over the IR region makes degenerately doped semiconductors interesting for optoelectronics, photonics, and biomedical applications.[12–14] Furthermore, most MOXs, such as ZnO, CdO, In_2O_3, and WO_3, are intrinsically n-type doped semiconductors due to the presence of oxygen vacancies; thus they exhibit LSPR features even when no external doping has been done.[2] The prime example of this is WO_{3-x} NCs.[15]

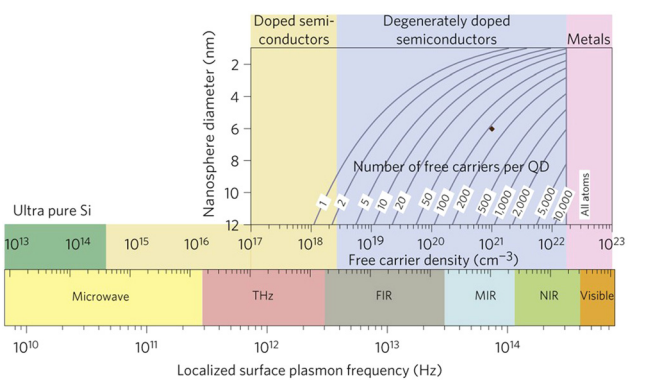

Fig. 1 Localized surface plasmon resonance (LSPR) frequency dependence on free carrier density and doping constraints. Reproduced from ref. 11 with permission from Springer Nature, copyright 2011.

[a] *Physics Department, Politecnico di Milano, Piazza L. da Vinci 32, 20133 Milano, Italy. E-mail: francesco.scotognella@polito.it*
[b] *Department of Applied Science and Technology, Politecnico di Torino, Corso Duca degli Abruzzi 24, Torino 10129, Italy. E-mail: giuseppemaria.paterno@polimi.it*

This review article is focused on highlighting the plasmonic properties of MOX NCs by reviewing the significant literature reported so far and their future prospective application in IR photodetectors and PV self-powered sensors. While reviewing the literature, we have tried to include all those reports in which interesting synthetic conditions or strategies were used to tune and improve the plasmonic properties of MOX NCs. We would like to point out that for a detailed and deeper understanding of different types of degenerately doped semiconducting materials and their fundamental plasmonic properties, readers can refer to the comprehensive review article by Milliron and collaborators.[2] Here, we first discuss the properties which make MOX NCs unique materials for harvesting light from a wide solar spectrum (UV-vis-IR) and provide an overview of the ultrafast charge-carrier dynamics along with the extraction of LSPR-assisted hot-carriers. Then, we present the most commonly used colloidal methods to synthesise NCs with relevant examples and review the comprehensive literature on degenerately doped indium oxide (In_2O_3), zinc oxide (ZnO), cadmium oxide (CdO) and tungsten oxide (WO_x) NCs. Finally, prospective applications of NCs in IR photodetectors and PV self-powered sensors are presented.

Observance of LSPR in IR extends the light-harvesting region of wide-band-gap MOXs: from UV through vis to IR

Wide-band-gap MOXs, such as ZnO, TiO_2, and In_2O_3, are generally transparent to visible light, with a band gap in the UV region.[16–18] Due to their strong absorption in UV, these materials have been immensely explored as UV-photodetectors[19,20] and are also employed to further enhance the efficiency of Si-solar cells by harvesting UV-light.[21] Furthermore, the band gap of MOXs can be tuned by varying the nanoparticle size and doping with different elements that provide the possibility of harvesting a wide range of UV light.

Recently, it has been observed that photogeneration of charge carriers occurs in MOXs under visible-light excitation.[22] This phenomenon is significantly explored in tuning the selectivity and response of gas sensors.[22,23] Q. Geng *et al.*[24] have illuminated ZnO with visible light ranging from 420 nm to 520 nm from an LED source and observed the sensing response owing to the photogenerated charge carriers. They have associated photogeneration in visible light with the phenomenon of two-photon or multi-photon absorption.[25,26] Detailed discussion of these phenomena is outside the scope of this review.

Finally, the LSPR in heavily doped MOX NCs in IR, which is the main topic of this review article, extends the light-harvesting capability of MOXs to the IR region. Later in the review article we will discuss the prospective application of MOX NCs for a future generation of IR-photodetectors and photovoltaic (PV) self-powered sensors due to their ability to harvest energy from a wider range of the solar spectrum (UV-vis-IR). However, to use degenerately doped MOX NCs for these two applications required a deeper understanding of their plasmonic dynamics under the illumination of IR-radiation and suitable device configuration for plasmon-assisted hot-carrier extraction. This leads us to our next section in which both these aspects are discussed.

Ultrafast dynamics in degenerately doped MOX NCs and extraction of hot carriers

The study of materials in different forms (gas, liquid, or solid) by means of ultrafast transient-absorption spectroscopy is of great interest as it provides useful information about the charge-carrier dynamics that occur at very short timescales (*e.g.* in femtoseconds), like plasmonic decay, plasmon-induced hot-carrier dynamics, exciton formation/dissociation, *etc.*[27–32] These types of investigations offer ultrafast signal manipulation with large variation in transmittance, which is very important for applications in active plasmonic, optical switching and all-optical signal-processing devices.[33–35]

In this regard, Kriegel *et al.*[36] investigated the ultrafast photodoping and plasmon dynamics in fluorine–indium co-doped CdO (FICO) NCs *via* pumping at 400 nm (band-gap excitation) and 1350 nm (LSPR excitation). The NCs were prepared by the heat-up method and the measurements were performed on a suspension of NCs in different solvents. Fig. 2 represents the transient-absorption (TA) response of FICO NCs to the intraband excitation of LSPR at 1350 nm. In particular, Fig. 2a shows the derivative-shaped TA spectra at a time-delay of 0.1 ps (left) along with the two-dimensional map of $\Delta T/T(\%)$ (right). Two types of contribution were observed: the maximum of the TA spectra (indicated by a broken blue line), represents photobleaching (PB) and photoinduced absorption (PA) is indicated by a broken red line. In Fig. 2b the decay of both PB and PA at 1580 nm and 1650 nm is shown. Two well-separated time-dependent dynamics were observed when NCs were excited with LSPR resonance: short-dynamics in the picosecond time range and longer-dynamics from 10 to 100 picoseconds. The initial fast decay (1 ps) is associated with the emission of phonons (carrier-phonons) and the slower decay corresponds to phonon–phonon scattering and the dissipation of heat into the solvent. It was also indicated that the initial fast decay was in fact even faster than that with noble metals due to the lower heat capacity and carrier concentration of semiconductor NCs. On the other hand, the TA dynamics of NCs after band-gap excitation (400 nm) is shown in Fig. 3. As shown in Fig. 3a, reverse dynamics as compared to LSPR excitation is observed. The PB maximum was observed at 1625 nm, while the negative signal (PA) showed a peak value at 1550 nm. Furthermore, the time axis in two-dimensional LSPR excitation (Fig. 2a) was up to 2 ps, while it was 10 ps in the case of 400 nm excitation, indicating that faster dynamics and signal modulation occurred when the NCS were excited at 1350 nm. A monoexponential decay in the signal was observed after the short rise time. The authors argued that pumping at

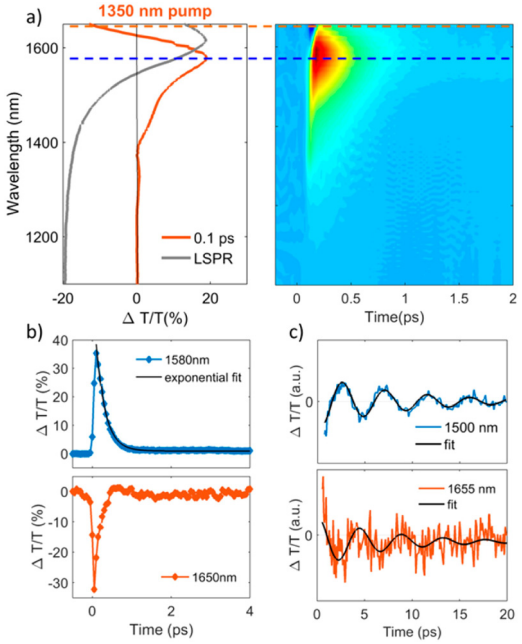

Fig. 2 Transient optical response of FICO NCs following intraband excitation. (a) Representative TA spectrum at the maximum rise time of around 100 fs after photoexcitation, exhibiting a derivative-shaped curve (left) together with the two-dimensional $\Delta T/T$ map (right), showing the signal as a function of pump–probe delay and probe wavelength for FICO NCs excited at 1350 nm with an excitation density of 0.13 mJ cm^{-2}. The steady-state LSPR absorption spectrum is also given in grey for comparison. (b) Transient decay dynamics at 1580 nm together with a biexponential fit (blue and black curves, respectively; upper panel, time constants of 0.23 and 38 ps) and 1650 nm (red curve, lower panel), illustrated by the horizontal cuts (dashed lines) depicted in panel (a). The time constant of the initial fast decay at 1650 nm is around 0.15 ps (not shown here). (c) $\Delta T/T$ time traces extracted at the selected probe wavelengths to the red (around 1655 nm) and the blue (1500 nm) of the maximum PB signal after subtracting the biexponential decay, along with their fits by a damped sinusoidal function (black curves). The extracted oscillating period is T = 4.4 ps, and the damping time constant is τ = 7 ps. Reproduced from ref. 36 with permission from ACS, copyright 2016.

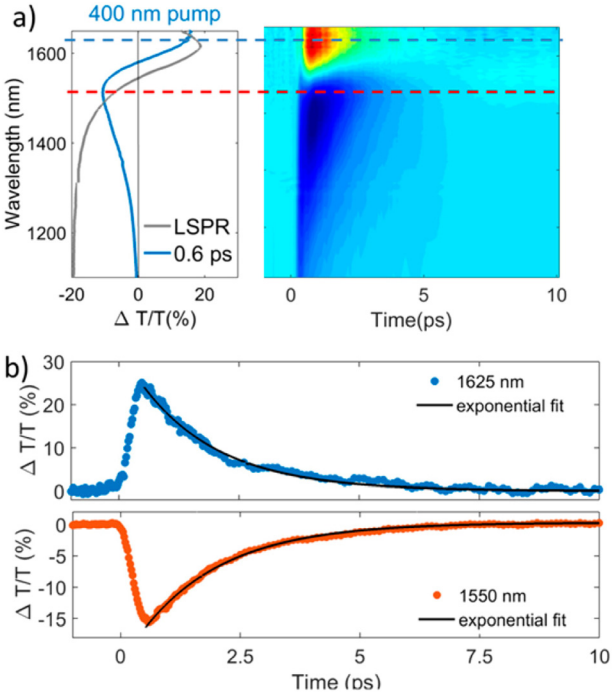

Fig. 3 Transient optical response of FICO NCs following intraband excitation. (a) TA spectrum at the maximum signal (0.6 ps) showing the typical derivative-shaped curve together with the two-dimensional $\Delta T/T$ map showing the signal as a function of pump–probe delay and probe wavelength for FICO NCs excited at 400 nm for the excitation density 2.35 mJ cm^{-2}. The steady-state LSPR absorption spectrum is also given in gray for comparison. (b) Transient decay dynamics at 1625 nm (blue curve upper panel) and 1550 nm (red curve lower panel) together with the monoexponential fits (black curve, time constant of 1.7 ps), illustrated by the horizontal cuts (dashed lines) depicted in panel a. Reproduced from ref. 36 with permission from ACS, copyright 2016.

400 nm results in the excitation of electrons to the conduction band, which increases the carrier density by capacitive charging. They proposed that the observed monoexponential decay is due to the temporarily increased carrier density after the ultrafast photodoping, which decays *via* electron–hole recombination.

In another study, In and Al-doped ZnO NCs were explored for ultrafast and broadband mid-infrared all-optical switching.[37] The In-doped ZnO NCs were synthesized using the heat-up method while the Al-doped ZnO NCs were synthesized using hot-injection. Briefly, by pumping NCs with LSPR resonance, picosecond all-optical Q-switching was realized with doped ZnO NCs in the MIR region from 3 to 5 μm.

Furthermore, the practical use these plasmonic properties of doped-MOX NCs relies mainly on the extraction of LSPR-assisted hot-electrons. However, hot-electrons exhibit very short lifetimes (tens of femtoseconds in metal[38] and hundreds of femtoseconds in doped oxide NCs[36]), making them difficult to extract. The extraction of these hot-carriers requires a suitable device structure or a junction with a suitable extraction layer. One such effort was made by M. Guizzardi *et al.*[39] in which the extraction of hot-carriers was done by fabricating a heterostructure between ITO NCs and a monolayer of molybdenum disulfide (MoS_2). The ITO NCs were synthesized by the continuous growth method and were transferred to the MoS_2 monolayer with spin-coating. Fig. 4 shows a depiction of the ITO/MoS_2 heterojunction and the band alignment between ITO and MoS_2. The heterostructure was pumped in resonance with the LSPR of

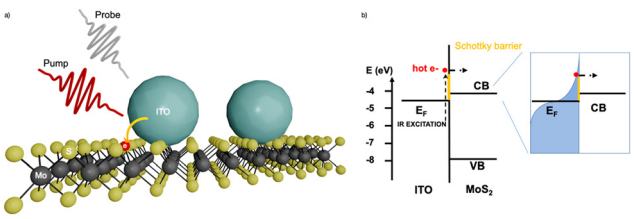

Fig. 4 (a) ITO/MoS_2 heterojunction sketch. (b) Band alignment between ITO and MoS_2; on the right-hand side, we have the sketch of the hot Fermi–Dirac distribution. Reproduced from ref. 39 with permission from ACS, copyright 2022.

ITO NCs at 1750 nm which was well below the band gap of MoS_2. By pumping the LSPR, a charge transfer from ITO to MOS_2 was observed that makes these types of heterostructure interesting for light-harvesting devices like infrared-solar cells.

After discussing plasmonic dynamics in NCs, we reach a point where it is necessary discus the synthetic approaches that are used to synthesize these plasmonic materials.

Synthesis of degenerately doped MOX NCs

Together with its obvious cost-effectiveness, solution-phase synthesis provides ease and flexibility for tuning the LSPR over the wide range of the IR region *via* chemical controls over (i) the incorporation of dopants inside the NCs, (ii) the type of dopant and (iii) the dopant concentration.[2] Among the different solution processable approaches like coprecipitation in aqueous solvents or reverse micelle templating, colloidal synthesis has gained significant attention owing to its ability to produce homogeneous NCs of many different materials including MOXs, thus becoming dominant over other synthetic routes.

For the synthesis of plasmonic MOX NCs, three main colloidal synthetic route routes have been very commonly used, namely:

(a) Hot-injection method.
(b) Heat-up method.
(c) Continuous growth method (slow injection).

The typical experimental setup for NC synthesis is composed of a three-neck round-bottom flask, a heating mantle with a temperature controller (inserted into the NC solution) and syringe for injection of the reactant. As the synthesis is done in under inert environmental conditions (*e.g.* in nitrogen), the middle neck is connected to a Schlenk line. A schematic of the setup is shown in Fig. 5a.[2]

Before we go into the detail of these methods, it is important to understand the nucleation and growth of NCs that were explained by LaMer and Dinegar in 1950.[40] In particular, they investigated the development of sulfur hydrosol for the slow decomposition of dilute sodium thiosulfate in dilute hydrochloric acid. Basically, it consists of three stages: monomer generation, nucleation and finally the growth of NCs (Fig. 5b).[2] In the first stage, the precursor is dissolved in the solvent and the reaction between them leads to the formation of a monomer.

The rate of monomer generation depends on the reaction kinetics and temperature. As the reaction proceeds, the concentration of monomer reaches its saturation level (C_s) and at this point nucleation does not start immediately as there is still a significant barrier to nucleation. However, when the monomer concentration reaches a certain minimum level (C_{min}^{nu}), nucleation starts spontaneously. During the accelerated growth of nuclei, the monomer is abruptly consumed. In fact, the monomer is formed by aggregation and self-nucleation processes. As the temporal formation of nuclei goes on, the monomer concentration reaches supersaturation and drops instantaneously. Indeed, the nucleation process stops when it reaches the C_{min}^{nu} level, which is the onset of the third and final stage: *i.e.* the growth of NCs *via* aggregation of monomers on pre-existing nuclei.

Now, let us come back to the three NC synthesis methods. All three methods are similar to each other as far as the overall process is concerned, but the major difference lies in the occurrence of nucleation and growth.[2]

Hot-injection method

The hot-injection method was first introduced by Bawendi *et al.*[41] in 1993 for the synthesis of CdE NCs in which E represents the three different elements: S, Se and Te. Afterwards, it was commonly used to produce high-quality NCs of a

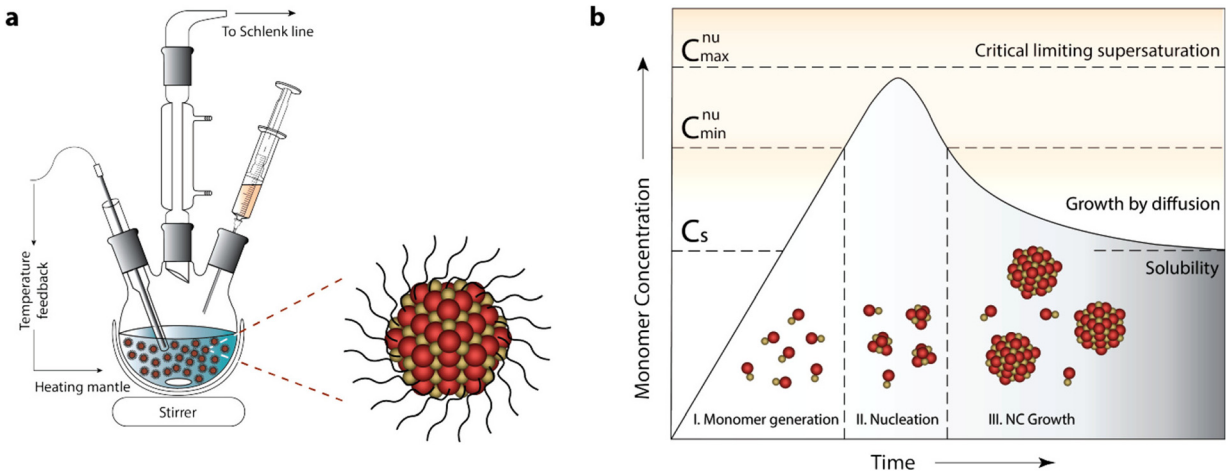

Fig. 5 General synthetic apparatus and growth model embodying the colloidal synthetic technique. (a) Schematic showing glassware and peripheral instrumental setup for a typical synthesis of surfactant-stabilized NCs, involving hot-injection. (b) LaMer–Dinegar model of colloidal NC formation. The three stages of monomer generation, nucleation, and growth are demarcated in the regions below the growth curve along with cartoons depicting the progression of the synthesis. Reproduced from ref. 2 with permission from ACS, copyright 2018.

variety of materials, including degenerately doped MOXs. As its name suggests, the precursor is quickly injected into a pre-heated solvent maintained in an inert environment under stirring. The central focus of hot-injection is to create single nucleation even after injection with successive growth of NCs that does not coincide with secondary nucleation. In other words, fast injection instantaneously starts the nucleation and the progression of the reaction leads to the formation of NCs. The solution also contains surfactant ligands that hinder agglomeration and determine the shape and size of the NCs. Notable surfactant ligands that have been used in the synthesis of NCs are long-chain carboxylic acids (oleic acid), alkylphosphine and alkylphosphine oxides (trioctylphosphine), and long-chain amines (oleylamine). Furthermore, by varying the growth temperature and time along with the surface concentration, NCs of different sizes and distributions can be achieved. In fact, as nucleation and growth occur separately, the hot-injection method offers high control over the size and size distribution of NCs.

With this method, Sirshendu Ghosh *et al.*[42] fabricated indium (In)-doped ZnO NCs in a nanopyramid shape, as shown in Fig. 6. The whole synthesis process is as follows: 2 mM of zinc acetylacetonate and indium acetate with different molar ratios were mixed with 2 mmol oleic acid and 5 mL of 1-octadecene (ODE) in a three-neck round-bottom flask. The mixture was first vacuumed at room-temperature and finally heated to 90 °C under the flow of Ar gas. Afterward, 15 mM of oleyl amine was dissolved in 1 mL of ODE and injected into the flask. The mixture was heated for 60 minutes at 240 °C, leading to the formation of In-doped ZnO NCs with broad LSPR in the IR region.

This method is extremely useful for applications in which precise control over the physical properties of NCs is required, *i.e.* the exploitation of LSPR. However, hot-injection is not useful for large-scale production, due to its dependency on the homogeneous mixing of reactants in a short period of time at high temperature; cooling can be inhomogeneous if the reaction is performed in a large reactor and a large volume of reactant cannot be injected abruptly, which can lead to the fabrication of inhomogeneous NCs with a broad range of sizes.[2]

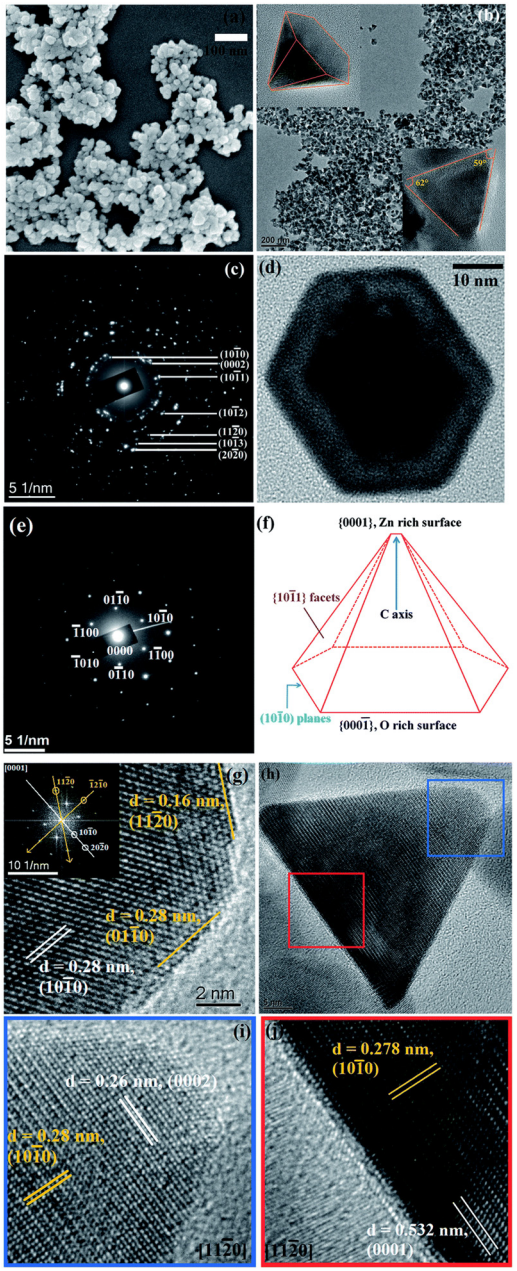

Fig. 6 (a) FESEM image of pure ZnO. (b) Low-resolution TEM image of the pure ZnO nanopyramid. The top-left and bottom-right insets of the figure depict the tilted (X = 41.1°, Y = 0°) and side views of a single ZnO hexagonal nanopyramid. (c) SAED pattern of the nanopyramid. (d) A single hexagonal pyramid viewed from the (0001) zone axis. (e) SAED pattern of a single nanocrystal. (f) Schematic presentation of a nanopyramid. (g) HRTEM image of a nanocrystal at the cross-section of two edges of the base. The inset shows the corresponding FFT pattern of the area. (h) Side view of a nanopyramid. (i) HRTEM image of the tip of the pyramid. (j) HRTEM image of the base of the pyramid. Reproduced from ref. 42 with permission from RSC, copyright 2014.

Heat-up method

Unlike hot-injection, heat-up is a non-injection method that involves the slow or steady heating of a precursor in the presence of a ligand. This method was first introduced by Hyeon *et al.*[43] in 2001 as an alternative to hot-injection, by which they synthesized monodispersed iron oxide nanoparticles. The experimental setup that describes the process of nanoparticle growth in comparison to the hot-injection method is shown in Fig. 7a, the scheme to synthesize nanoparticles in Fig. 7c, a photograph of Taeghwan Hyeon and Jongnam Park in Fig. 7e, and TEM images of iron oxide nanoparticles with different sizes are shown in Fig. 7b, d, and f–h.[44] As shown in Fig. 7a, the mixture of precursor, surfactants and solvents is heated to first initiate the nucleation and then the growth of NCs. Hyeon *et al.*[43] undertook the decomposition of iron pentacarbonyl in the presence of oleic acid at 100 °C, leading to the generation of an iron–oleic acid metal complex. This metal complex was then further heated to 300 °C (aging), eventually forming iron nanoparticles. To oxidize these iron

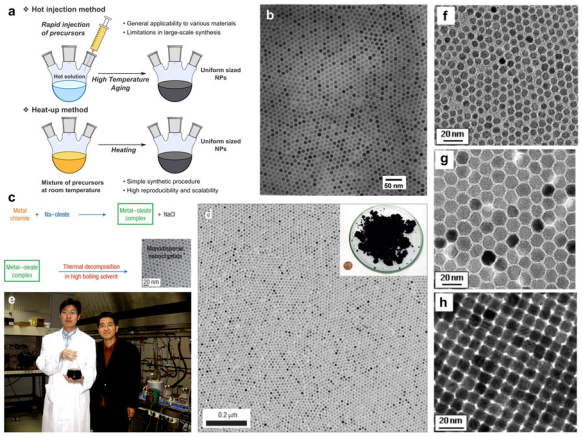

Fig. 7 (a) Schematic illustration of the hot-injection method and heat-up method for uniform-sized nanoparticles. (b) Transmission electron microscopy (TEM) image of 11 nm γ-Fe_2O_3 nanoparticles. (c) The overall scheme for the synthesis of monodispersed nanoparticles through metal–oleate complexation. (d) TEM image of 12 nm Fe_3O_4 nanoparticles. Inset is a photograph of 40 g of the monodispersed Fe_3O_4 nanoparticles, and a US one-cent coin for comparison. (e) Photograph of Taeghwan Hyeon and Jongnam Park in 2004. (f)–(h) TEM images of (f) 6 nm, (g) 12 nm, (h) 10 nm monodispersed Fe_3O_4 nanoparticles. Reproduced from ref. 44 with permission from Wiley, copyright 2023.

NCs to form iron oxide NCs, trimethylamine oxide was added into the mixture as an oxidant agent. In the heat-up method, the nucleation step lasts longer than in hot-injection because of the continued generation of monomers caused by the sustained supply of heat. This leads to an overlap between the nucleation and growth stages: in fact, additional nucleation can also happen during the growth of the initial nuclei. Hence, a high degree of control over size and shape is sometimes difficult with this method, due to the overlap between the nucleation and growth stages. The main advantage of the heat-up method is its scalability, as no injection step is involved and all the reactants are mixed up and heated together to generate high-quality NCs.

Continuous growth method

In a continuous growth method, the precursor is slowly injected into the solution pre-heated to a certain temperature. Hence, this method is intermediate between the hot-injection and heat-up methods. The slow and continuous injection of precursor allows the growth of well-sized and uniform NCs because of the layer-by-layer layer deposition of monomer on the NC surface. Hence, this method is useful for synthesizing core–shell NCs, in which the core and shell are made up of different materials like CdSe/ZnS core–shell NCs. Using this method, Fe, Co, Cu and Zn doped In_2O_3 NCs were synthesized.[45] Briefly, a metal–oleate precursor was prepared by mixing 1 mM indium(III) acetate and a specific amount of dopant precursors in 2 mL of oleic acid in a vial which was then heated at 150 °C in an oil bath under an N_2 environment for 1 hour. In the case of doping with Fe, the heating was done at 190 °C. After completion of the reaction, this solution was slowly injected (0.35 mL min^{-1}) into 13 mL of oleyl alcohol and heated to 290 °C under an N_2 environment. The TEM images of doped In_2O_3 NCs are shown in Fig. 8.

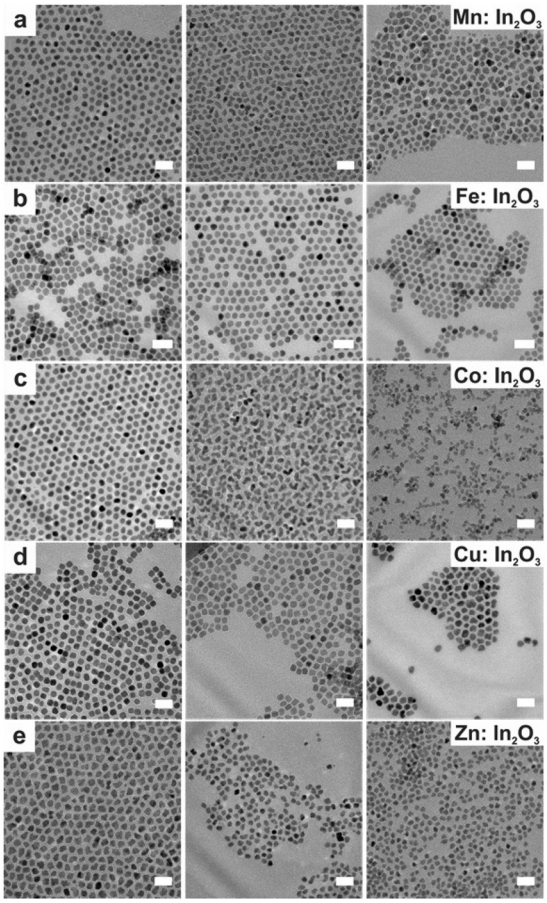

Fig. 8 TEM images taken of doped In_2O_3 nanocrystals at varying molar dopant ratios. Scale bars are 20 nm. The nominal dopant percent in the precursor increases from left to right, 5% dopant on the left, 10% center, and 20% right: (a) Mn:In_2O_3, (b) Fe:In_2O_3, (c) Co:In_2O_3, (d) Cu:In_2O_3, and (e) Zn:In_2O_3. Reproduced from ref. 45 with permission from ACS, copyright 2017.

Progress in MOX NCs

After the discussion on synthetic approaches, we will now review the literature on different MOX NCs and explore their plasmonic properties. In particular, we will focus on how different experimental conditions or strategies like the use of different dopants, doping levels, or temperature of growth can influence their LSPR in the IR region.

In_2O_3-based nanocrystals

Thanks to its great use as a transparent conducting oxide (TCO) for devices like solar cells, Sn-doped In_2O_3 (ITO) remains the most studied and investigated plasmonic MOX.[46–49] In fact, degenerately doped In_2O_3 NCs are used as a model to investigate and understand phenomena such as defect engineering,[50] dopant distribution,[51] or dopant selection.[52] In an interesting

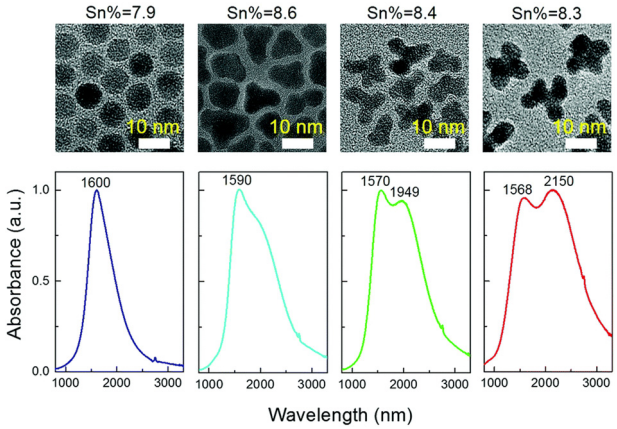

Fig. 9 Solution-phase UV-vis-IR absorbance spectra of four shapes (spheres, triangles, tripods and tetrapods) of Sn-doped nanocrystals in CCl_4. The nominal doping concentration is the same (8%) for all the samples and the real doping concentrations are 7.9%, 8.6%, 8.4%, and 8.3%, respectively, determined by ICP-AES techniques. Reproduced from ref. 53 with permission from RSC, copyright 2017.

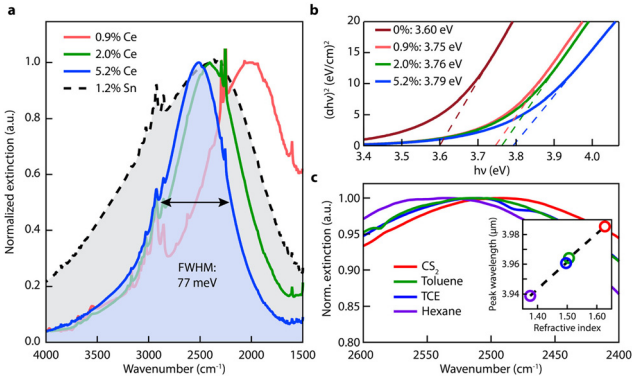

Fig. 10 Optical properties of Ce:In_2O_3 nanocrystals. (a) FTIR liquid cell spectra of Ce:In_2O_3 and Sn:In_2O_3 nanocrystals dispersed in tetrachloroethylene showing narrow and tunable MIR LSPR of Ce:In_2O_3. (b) Tauc plots showing systematic increase in Ce:In_2O_3 optical band gap with Ce content, consistent with a Burstein–Moss shift. (c) LSPR of 5.2% Ce-doped In_2O_3 dispersed in nonpolar solvents with different refractive indices. Inset: LSPR peak wavelength *versus* refractive index. Reproduced from ref. 50 with permission from ACS, copyright 2016.

report, Yu Gu *et al.*[53] synthesized triangle-, tripod-, and tetrapod-branched ITO NCs with the heat-up method for anisotropic infrared plasmonics. Fig. 9 shows the UV-vis-IR spectra along with the TEM images. Clearly, the LSPR characteristics of NCs are strongly correlated with the shape of the NCs. In particular, beside the spherical ITO NCs, an additional component appears at a lower plasmon energy, which is also intensified and shifts towards lower energy (red shift) with an increase in anisotropy of NC shapes. Conversely, the LSPR peak at high energy is slightly blue-shifted. In order to understand the shape dependence of LSPR characteristics, finite-difference time-domain (FDTD) simulation was performed. Detailed analysis shows that the low-energy and high-energy peaks are attributed to in-plane and out-of-plane polarization. In-plane polarization is responsible for excitation of the A_2'' mode (triangles and tripods) of the D_{3h} point group and the A_{2u} mode (tetrapods) of the D_{4h} point group. On the other hand, the out-of-plane mode is related to the E′ mode (triangles and tripods) of the D_{3h} point group and the E_u mode (tetrapods) of the D_{4h} point group. Apart from the shape of the NCs, the dopant distribution is also found to affect their plasmonic properties.[51] Fig. 10a shows the optical extinction coefficient of ITO NCs at different doping levels of Sn and XPS depth profiling of Sn in NCs (Fig. 10b). Clearly with a doping content up to 5.1%, a gradual increase in peak intensity and blueshift is observed. But, when the Sn doping content further increases to 7.6%, a redshift is observed, which is an indication of the formation of irreducible Sn complexes along with interstitial oxygen atoms. Furthermore, the surface Sn content exhibits a linear relationship up to an Sn doping content of 5.1% (see Fig. 10b). This is attributed to the uniform distribution of dopant (Sn) in the NCs. But when the doping level further increases, an abrupt increase in surface Sn content is observed for 650 eV photons compared to 1150 eV photons. This indicates the surface segregation of Sn at a higher doping level.

Furthermore, in another interesting piece of work by Milliron *et al.*[50] cerium (Ce)-doped In_2O_3-based NCs were proposed. To synthesize Ce:In_2O_3 NCs, indium acetylacetonate, cerium precursor, and OLA were mixed in a three-neck round-bottom flask, connected to a Schlenk line and heated to 250 °C for 2 h in an inert environment. Fig. 11 represents the optical characterization of Ce:In_2O_3 NCs with the different doping contents of Ce. As shown in Fig. 11a, the Ce:In_2O_3 NCs exhibit a narrow LSPR peak compared to ITO NCs with the peak shifted to higher energy with an increase in the Ce content. Furthermore, the band gap of the NCs was also found to increase with an increase in Ce doping. Further, when dispersions of NCs were made in different nonpolar solvents (with increasing refractive index), a redshift in the LSPR peak was observed (see Fig. 11c). Additionally, Ce:In_2O_3 NCs were found to exhibit an electron mobility value of 33 $cm^2\ V^{-1}\ s^{-1}$, higher than that of ITO NCs, making them ideal for transparent conducting applications. Furthermore, S. H. Cho *et al.*[54] synthesized fluorine (F), Sn co-

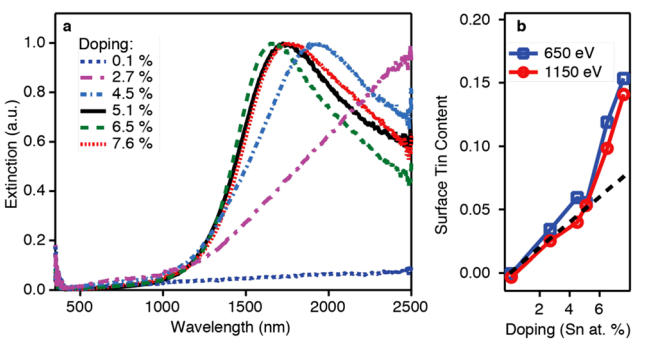

Fig. 11 (a) Optical extinction and (b) XPS depth profiling *versus* doping for the doping series. The dotted black line in panel (b) shows the expected Sn/(In + Sn) ratio for a uniform doping profile. Reproduced from ref. 51 with permission from ACS, copyright 2014.

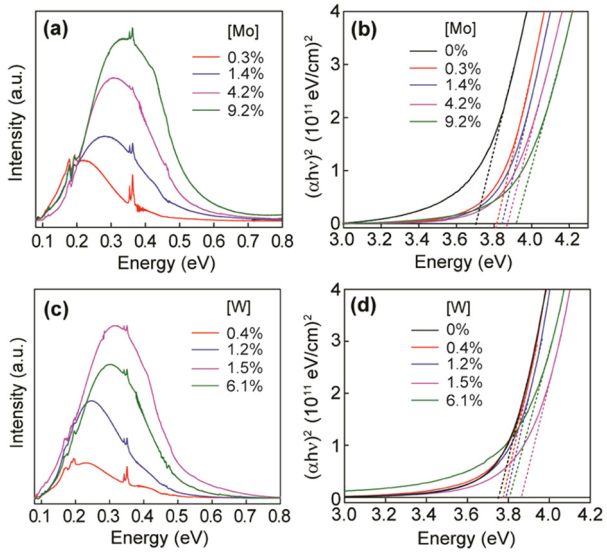

Fig. 12 (a) LSPR absorption spectra of IMO NCs with different doping concentrations, as indicated in the graph. (b) Tauc plots for IMO NCs from panel (a) used to determine optical band gaps. (c) LSPR absorption spectra of IWO NCs with different doping concentrations, as indicated in the graph. (d) Tauc plots for IWO NCs from panel (c) used to determine optical band gaps. Reproduced from ref. 55 with permission from ACS, copyright 2019.

doped In_2O_3 NCs with the hot-injection method. The co-doped NCs exhibit LSPR characteristics in the NIR region.

Furthermore, molybdenum (Mo) and tungsten (W) were also incorporated into In_2O_3 and showed LSPR in the mid-IR region.[55] To synthesize Mo and WO doped In_2O_3 NCs (IMO and IWO), the metal/dopant precursors were mixed with OLA and heated at 250 °C and 300 °C, respectively. Fig. 12 shows the LSPR absorption spectra and Tauc plots of IMO and IWO NCs. Clearly, both NCs exhibit LSPR in the mid-IR region with the peak shifted to higher energy with an increase in the doping content of Mo and W. Furthermore, the band gap also increases with an increase in doping due to the Burstein–Moss effect. Similarly, antimony (Sb) and titanium (Ti) doped In_2O_3 NCs exhibit LSPR in the mid-IR region.[56] At a similar doping level of Sb and Ti, the LSPR of Ti-doped NCs was found to be at lower energies and possessed smaller bandwidths compared to Sb-doped In_2O_3 NCs. This indicates the lower density of free electrons in Ti-doped In_2O_3 NCs. In an impressive study, the synthesis of zirconia (Zr)-doped In_2O_3 NCs *via* a hot-injection method was described for the first time.[52] By calculating the quality factor (*Q*-factor) of LSPR, which is defined as the ratio of LSPR peak energy to its line width, the authors represented the dopant selection criteria. It was found that for high LSPR energy, a stable oxidation state and deeper donor state in the conduction band of the host are required. While for small LSPR, the full width at half maximum (FWHM) requires a higher charge/radius ratio and lower electronegativity of the dopant cation corresponding to the host cation. In this regard, Zr is found to be an ideal aliovalent dopant for In_2O_3 as it exhibits the highest *Q*-factor compared to any other plasmonic material reported in the literature so far. The FTIR spectra of Zr-

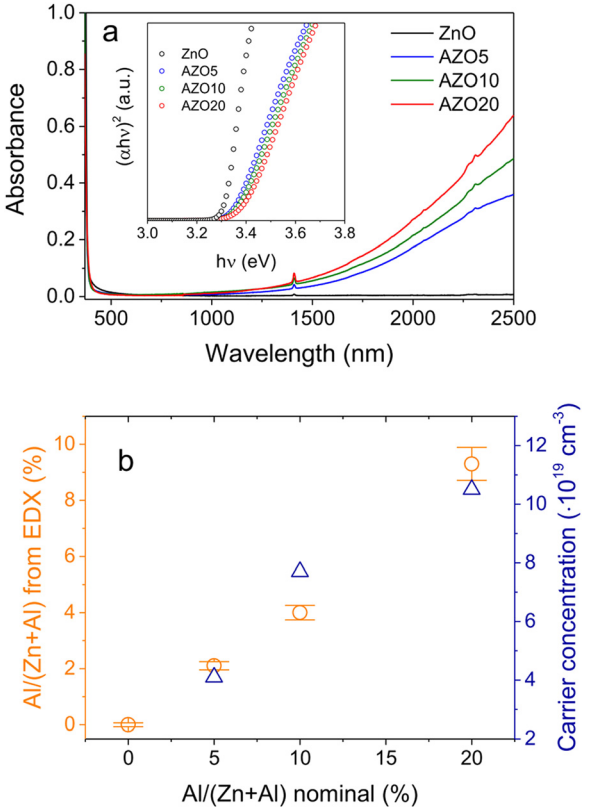

Fig. 13 Synthesis of Al-doped ZnO NCs. (a) UV-vis-NIR spectra of ZnO NCs doped with different amounts of Al. The inset shows the respective Tauc plots. (b) Charge-carrier concentration evaluated from the LSPR frequency and nominal *vs.* real (from EDX) Al concentration for ZnO NCs doped with different amounts of aluminum. Reproduced from ref. 57 with permission from ACS, copyright 2019.

doped In_2O_3 NCs with different doping contents and the corresponding *Q*-values are shown in Fig. 13. Clearly, the NCs showed LSPR fingerprints in the mid-IR region.

ZnO-based nanocrystals

Among all the different MOXs, ZnO remains the centre of interaction after ITO for optoelectronics owing to its large exciton binding energy which is 60 meV.[58] In particular, AZO is regarded as a leading candidate for the replacement of ITO as a transparent conducting oxide (TCO).[59] Due to its remarkable optoelectronics properties, continuous effort has been made to obtain and tune the LSPR over a wide range of the IR region by incorporating different dopants, such as Al, In, Ge, or Ga.

P. Wainer *et al.*[57] synthesized Al-doped ZnO NCs with continuous growth methods. In a typical synthesis, the solution of metal precursor and dopant was first prepared in oleic acid (OA) and oleylamine (OLA), which was then slowly injected (3 mL min^{-1}) into preheated oleyl alcohol. Fig. 14a shows the UV-vis-NIR spectra (the inset indicates the band gap) of pristine and Al-doped ZnO (AZO) NCs with different dopant percentages (AZO5: 5%Al, AZO10: 10%Al and AZO: 20%Al). Clearly, the AZO NCs exhibit LSPR in the NIR region whose intensity was found to increase with an increase in doping

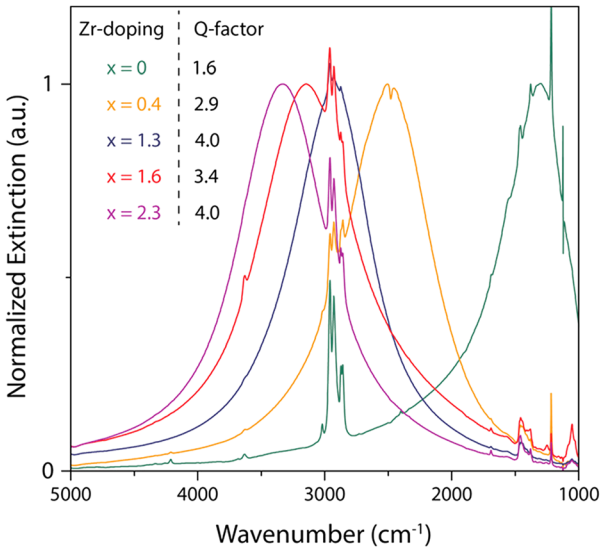

Fig. 14 Optical extinction spectra of different Zr:In_2O_3 NCs displaying narrow and symmetric LSPR bands increasing in energy with an increase in Zr doping. Spectra were taken by FTIR of NCs dispersed in tetrachloroethylene. Reproduced from ref. 52 with permission from ACS, copyright 2019.

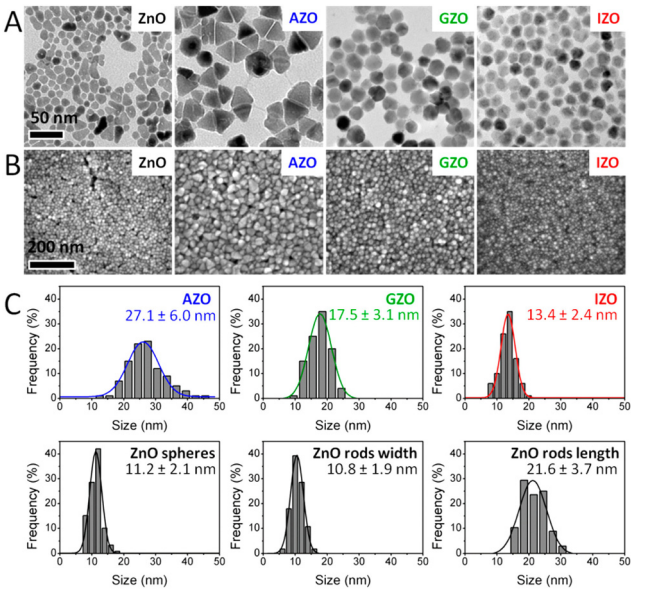

Fig. 15 Electron microscopy characterization of ZnO-based NCs. (A) TEM images (the scale bar is the same in all TEM images). (B) SEM images (the scale bar is the same in all SEM images). (C) Histograms of size distribution evaluated from TEM images. Reproduced from ref. 60 with permission from the authors: E. Della Gaspera, and J. J. Jasienia, ACS copyright 2014.

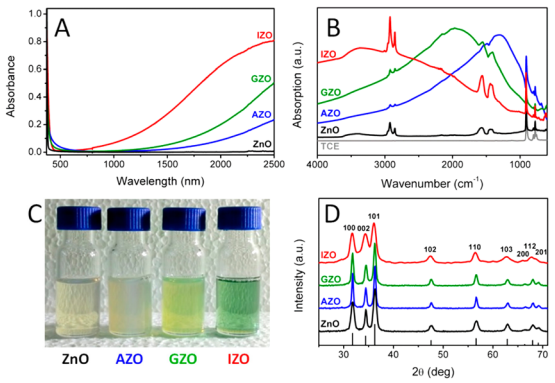

Fig. 16 (A) Optical absorption spectra of equimolar solutions of ZnO-based NCs in TCE. (B) FTIR spectra of the same colloidal solutions. (C) Photograph of the concentrated stock solutions (absorption spectra are obtained by diluting the stock solutions ~50 times). (D) XRD patterns of the dried powders (the predicted diffraction peaks for bulk wurtzite ZnO are displayed at the bottom). Reproduced from ref. 60 with permission from the authors: E. Della Gaspera, and J. J. Jasienia, ACS copyright 2014.

concentration. Additionally, the band gap is also found to increase with dopant concentration due to the Burstein–Moss effect. Furthermore, a carrier concentration up to 10^{20} cm^{-3} was achieved with the highest doping level of aluminium (see Fig. 14b). Indeed, the authors were able to incorporate 40% of Al into ZnO NCs. In another interesting study, ZnO NCs doped with In, Ga and Al were prepared by a non-injection method (heat-up).[60] Initially, precursors (metal and dopant), surfactant and solvent were mixed together in a nitrogen atmosphere at 100–140 °C and then the temperature was gradually increased to 250 °C at a rate of ~4 °C min^{-1}, leading to the formation of NCs. In Fig. 15, the surface morphologies of ZnO, AZO, Ga-doped ZnO (GZO) and In-doped ZnO (IZO) NCs along with their size distributions are shown. As can be seen from the TEM images, NCs seemed to exhibit both spherical and elongated shapes (and also a few rod-like ones). The sizes of ZnO, AZO, GZO and IZO were found to be 11.2 ± 2.1 nm, 27.1 ± 6.0, 17.5 ± 3.1, and 13.4 ± 2.4 nm, respectively. Furthermore, optical characterization (UV-vis-NIR and FTIR) of all the NCs along with a photograph of the stock solution and their XRD patterns are shown in Fig. 16. Apart from undoped ZnO NCs, all the doped NCs exhibit LSPR in the NIR region. The FTIR study reveals that the LSPR of AZO, GZO, and IZO showed peak values at 7.5, 5, and 3 μm. According to Drude–Lorentz theory, the frequency of LSPR resonance can be related to the charge-carrier density (n) by the following equation:

$$n = \omega^2 m_e e_0(\varepsilon_\infty + 2\varepsilon_m)/e^2$$

where ω is the resonance angular frequency of LSPR in the NCs, m_e is the electron effective mass (9.11×10^{-31} kg), ε_0 is the permittivity of free space (8.854×10^{-12} F m^{-1}), ε_∞ is the high-frequency dielectric constant which is 3.71 for ZnO, ε_m is the dielectric constant of the medium surrounding the NCs, *e.g.* the solvent in which the NCs are dispersed, and e is the electron charge, 1.6×10^{-19} C. This equation clearly indicates that the LSPR resonance frequency ω is directly proportional to the carrier concentration n (and inversely proportional to wavelength). In the present case, the carrier concentrations for AZO, GZO, and IZO NCs were found to be ~4.2×10^{19}, ~9.4×10^{19}, and ~2.6×10^{20} cm^{-3}, respectively. Thus, due to the highest carrier concentration in IZO NCs, their LSPR resonance appears at lower wavelength than for other doped NCs. Moreover, all the

NCs possessed a typical wurtzite structure, as shown in the XRD spectra (Fig. 16D). Furthermore, size and dopant controlled AZO NCs were synthesized by Milliron *et al.*[9] In this work, the use of coordinating ligands in the synthesis process provides the control over the reaction between metal and dopant precursors that in turn helps to tune the Al doping content in the NCs from 0 to 8%. While changing the growth temperature helps to maintain the size of the NCs between 5 and 20 nm. To synthesize AZO NCs, a precursor solution containing 1 mM zinc stearate ($ZnSt_2$), 0.05–0.5 mM aluminium acetylacetonate ($Al(acac)_3$), and 3 mL of OA in 4 mL of octadecene (ODE) was injected into a solution of 10 mL of 1,2-hexadecanediol (HDDIOL) in 11 mL of ODE which was preheated to 230–260 °C. The reaction was performed in an inert argon environment. After the addition of precursor solution, the temperature was found to drop by 20 °C, leading to the formation of narrow-sized NCs. While a gradual increase in temperature led to the formation of bigger NCs. Fig. 17 shows the TEM images of NCs grown at different temperatures, *i.e.* at 230 °C (Fig. 17A), 240 °C (Fig. 17B) and 260 °C (Fig. 17C). Furthermore, all the AZO NCs doped with different Al content exhibit LSPR in the NIR region. With an increase in the doping content of Al, the intensity of IR absorption increased monotonically and the LSPS resonance shifted to high energy (towards lower wavelength). In another interesting piece of work, M. Saha *et al.*[61] reported the hot-injection synthesis of hexagonal-shaped trivalent Ga-doped ZnO NCs (GZO). The UV-vis-NIR and FTIR spectra of GZO NCs are shown in Fig. 18. As shown in Fig. 18a, all GZO NCs exhibit LSPR characteristics in the NIR region and up to a doping content of Ga of x = 0.02, the peak intensity monotonically increased. However, with a further increase in doping content to x = 0.04, a concomitant decrease in the IR absorption was observed. The authors associate this decrease with three possible reasons: (i) inhomogeneous doping of Ga; (ii) electron trapping around the Ga^{3+} ion; (iii) obliteration of the NC size distribution. These results indicate that the doping content must be carefully optimized to obtain strong LSPR characteristics. Furthermore, Gaspera *et al.*[62] synthesized germanium (Ge)-doped ZnO colloidal NCs for the very first time by employing the heat-up method. In a typical synthesis, the Ge precursor [*i.e.* Ge(*O*,*O*′-glycolate)$_2$(H_2O)$_2$] was dissolved in OLA at 120 °C under cooling. After cooling the Ge precursor solution, it was added into the $ZnSt_2$ solution in a mixture of OA, 1-dodecanol and ODE. After the addition, the solution was heated at 230 °C for 2 hours, leading to the formation of Ge-doped ZnO NCs. The UV-vis-NIR absorption spectra of Ge-doped ZnO NCs are shown in Fig. 19a along with the Tauc plots in Fig. 19b. All the doped NCs exhibit LSPR in the NIR region, which increases with an increase in the doping level of Ge. On the other hand, the band gap is also found to increase with an increase in doping content which is an indication of the Burstein–Moss effect. Fig. 19c is a representation of the band gap with an increase in the doping level of Ge in ZnO NCs. In similar work, W. Zhu *et al.*[63] investigated the change in the structure and composition caused by Ge doping in ZnO NCs. Again, the ZnO NCs were fabricated using the heat-up method and their thin film was deposited by spin-coating. Detailed investigation reveals that degenerate doping of ZnO NCs with Ge reduces the intrinsic defects in ZnO and suppresses the emission in the green–red region from defects and free excitons. The suppression of emission was found to be caused by the substitution of Ge^+ at Zn sites and the formation of non-radiative deep-level traps $(GeZn)^+$.

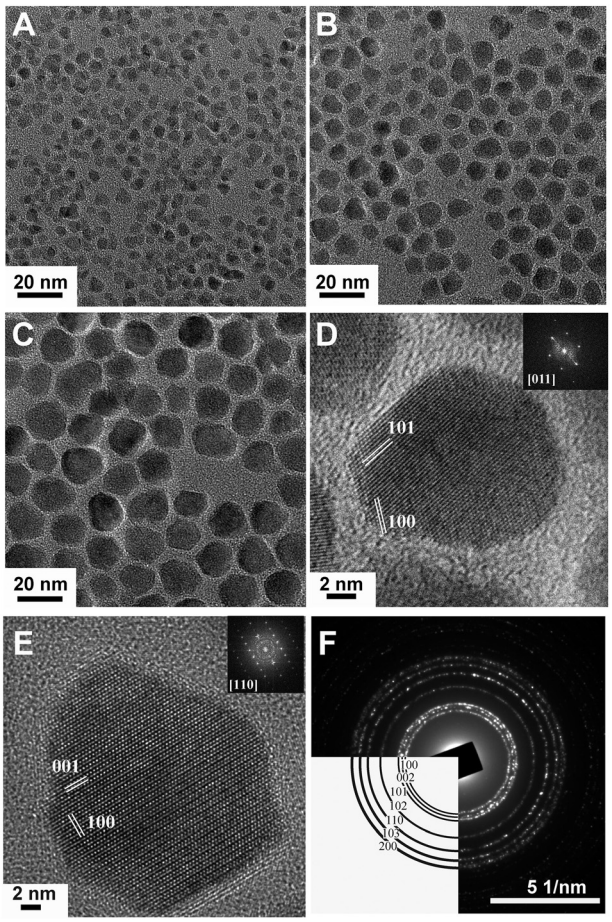

Fig. 17 Low- and high-resolution TEM images of AZO NCs. (A)–(C) AZO NCs of different sizes were obtained by injecting precursor solutions containing 0.2 mmol of $Al(acac)_3$ at 230, 240, and 260 °C, respectively. (D) HRTEM image of a pseudospherical AZO NC oriented along the [011] zone axis and the corresponding fast Fourier transform (FFT) in the inset indicating the hexagonal structure of the wurtzite. The lattice fringes correspond to spacings of 2.42 and 2.79 Å derived from FFT which match well the *d* spacing of the (101) (d^{101}_{ZnO} = 2.47 Å) and (100) planes (d^{100}_{ZnO} = 2.81 Å) of wurtzite ZnO. (E) HRTEM image of a bullet-shaped AZO NC oriented along the [110] zone axis and the corresponding FFT in the inset. The lattice fringes correspond to 2.79 and 2.58 Å, derived from FFT, consistent with the (100) and the (001) (d^{001}_{ZnO} = 2.60 Å) planes, respectively, of wurtzite ZnO. (F) Electron diffraction of AZO NCs with the expected wurtzite pattern indicated in the lower left. Reproduced from ref. 9 with permission from ACS, copyright 2011.

WO_{3-x}-based nanocrystals

The reduced form of WO_3, *i.e.* WO_{3-x}, exhibits strong LSPR features in the NIR region,[64–68] owing to the presence of oxygen vacancies in the crystal lattice.[69] WO_{3-x} possesses a strong blue

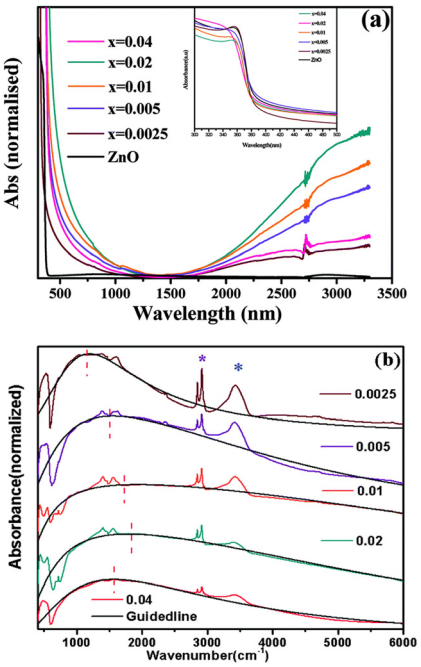

Fig. 18 (a) Optical absorption spectra of pure ZnO and doped $Zn_{1-x}Ga_xO$ nanocrystals in the vis-NIR region. The inset depicts the band-gap absorption of the samples. (b) FTIR spectra of doped samples showing the plasmonic NIR absorption. Additional sharp peaks (asterisks) arise from the organic ligand oleylamine absorbed on the nanocrystal surface. Blue and purple asterisks represent N–H stretching and symmetric/asymmetric stretching vibration of long hydrocarbon chains, respectively. The black dotted line and the red vertical dotted line are guiding lines for the shifting of plasmonic absorption. Reproduced from ref. 61 with permission from RSC, copyright 2015.

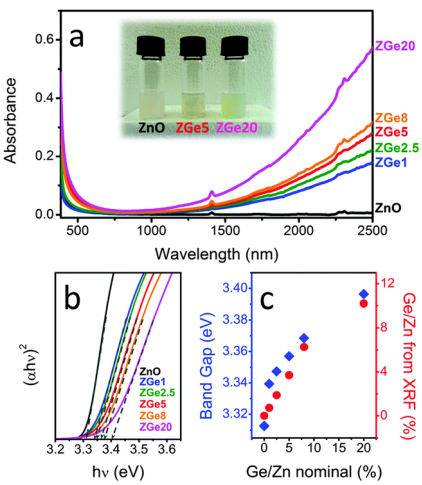

Fig. 19 (a) Optical absorption spectra of equimolar colloidal solutions of ZnO:Ge in tetrachloroethylene (TCE). The inset shows a digital photograph of the prepared colloidal solutions. (b) Tauc plots (exponent = 2, direct band gap) of the ZnO:Ge colloidal solutions. The dashed lines are the linear fits used to identify the band gap. (c) Optical band gap and real Ge/Zn amount evaluated from XRF as a function of the nominal Ge/Zn ratio. Reproduced from ref. 62 with permission from RSC, copyright 2015.

colour and can be obtained in a variety of stoichiometries, *i.e.* $WO_{2.83}$ ($W_{24}O_{68}$), $WO_{2.72}$ ($W_{18}O_{49}$), $WO_{2.8}$ (W_5O_{14}) and $WO_{2.9}$ ($W_{20}O_{58}$).[15] K. Manthiram *et al.*[15] synthesized nanorod-shaped $WO_{2.83}$ NCs *via* the hot-injection method with tuneable LSPR. Fig. 20 shows the UV-vis-NIR spectra of a $WO_{2.83}$ nanorod suspension in *N*-methylpyrrolidone (Fig. 20a), along with its crystalline properties (Fig. 20b). In particular, in Fig. 20b, the LSPR features of $WO_{2.83}$ nanorods heated at 175 °C for 0, 2 and 6 minutes are presented. Clearly, upon heating, the intensity of the LSPR peak is decreased and peak is shifted to higher wavelength (redshift), due to the decrease in carrier concentration caused by the oxidation of $WO_{2.83}$. On the other hand, the absorption edge exhibits a blueshift upon heating. Furthermore, a decrease in the crystallinity of the nanorods is observed when heated at 175 °C for 6 minutes. In another study, cesium-doped tungsten oxide (Cs_xWO_3) NCs were prepared and explored to evaluate their plasmonic properties.[69] These types of interstitially doped tungsten oxide are also known as tungsten bronze with the formula M_xWO_3 (M: Li^+, Na^+, Cs^+, or Rb^+). In Fig. 21, we report the TEM images of pristine $WO_{2.72}$ nanorods and Cs_xWO_3 NCs prepared by the group of Delia Milliron, and exhibiting three different shapes: hexagonal prism, truncated cube, and pseudospheres. These doped NCs exhibit LSPR in the NIR region. Furthermore, WO_{3-x} NCs prepared by solvothermal methods showed string plasmonic behaviour in the vis-NIR region.[70] Fig. 22 shows the UV-vis-NIR absorbance spectra of WO_{3-x} NCs in protic polar solvents. In the case of NCs dispersed in ethanol, an extremely well-resolved plasmonic peak at 556 nm was observed.

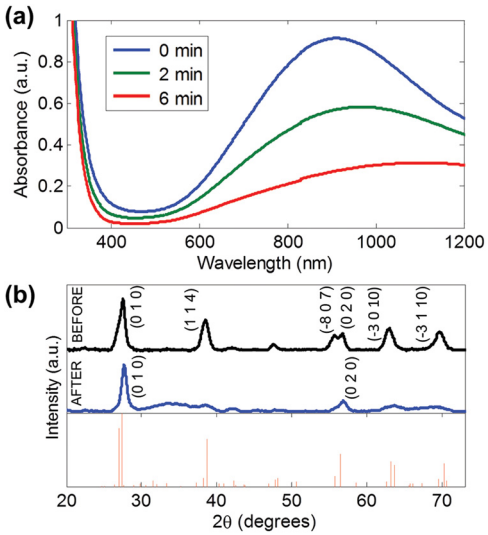

Fig. 20 (a) UV-vis-NIR absorption spectra of $WO_{2.83}$ nanorods in *N*-methylpyrrolidone upon heating at 175 °C in air for 0, 2, and 6 min. (b) XRD patterns of $WO_{2.83}$ nanorods in *N*-methylpyrrolidone (top) before and (middle) after heating at 175 °C for 6 min in air and (bottom) the reference pattern for $WO_{2.83}$. Reproduced from ref. 15 with permission from ACS, copyright 2012.

CdO-based NCs

Cadmium oxide (CdO) is another n-type wide-band-gap MOX that showed LSPR with[71,72] or without doping.[73] Fig. 23 shows the TEM images of octahedral-shaped In-doped CdO (ICO) NCs

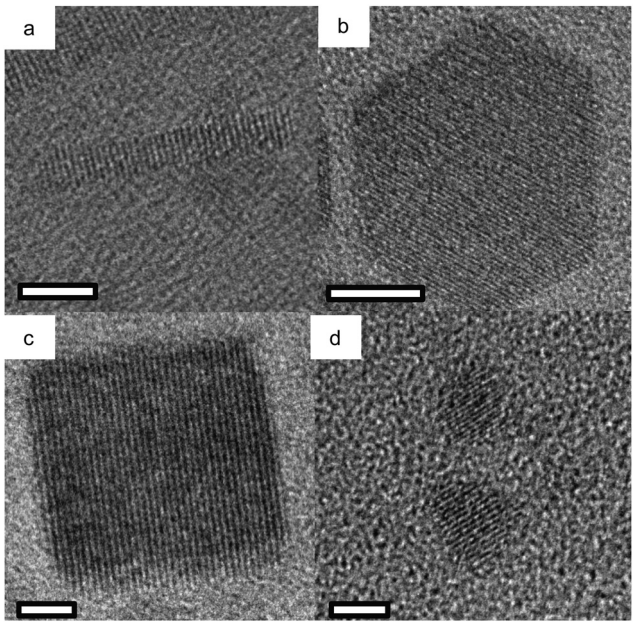

Fig. 21 High-resolution TEM images of (a) $WO_{2.72}$ rods and Cs_xWO_3 (b) hexagonal prism, (c) truncated cube, and (d) pseudospheres. All scale bars are 5 nm. Reproduced from ref. 69 with permission from ACS, copyright 2014.

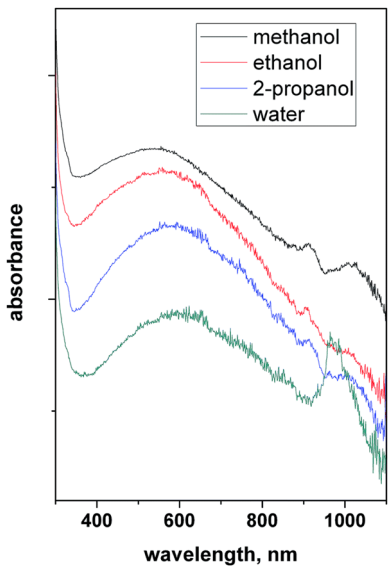

Fig. 22 UV-vis-NIR absorbance of WO_{3-x} nanocrystals – LSPRs in different protic polar solvents. Reproduced from ref. 70 with permission from RSC, copyright 2016.

along with a pictorial representation of the ICO unit cell.[71] This was the first report on ICO NCs synthesized using the heat-up method in both spherical and octahedral shapes. As can be seen from Fig. 23, compatibly larger ICO NCs were formed when the oleic acid (OA) concentration was 3 mM. Furthermore, the absorption spectra indicating the LSPR feature of ICO NCs (from NIR to MIR) and band gap at different doping contents of In (see Fig. 24). With an increase in In-doping content, the LSPR peak is blue-shifted. Additionally, as

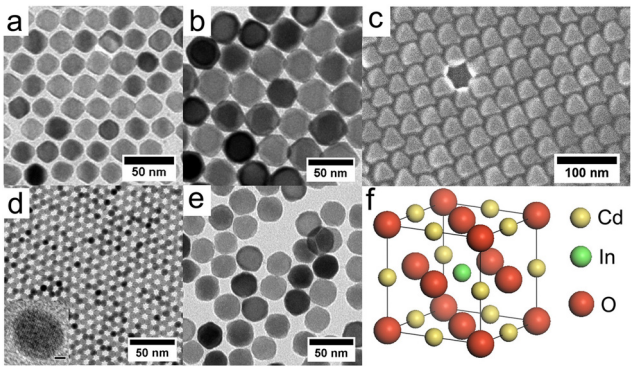

Fig. 23 TEM images of octahedral ICO nanocrystals produced at 300 °C using (a) 4 mmol and (b) 3 mmol OLAC and (c) SEM image of the sample shown in b. TEM image of spherical nanocrystals produced at reflux using (d) 5 mmol and (e) 3 mmol OLAC. (f) The unit cell of rock-salt type indium-doped cadmium oxide (ICO). Influence of Shape on the Surface Plasmon Resonance of Tungsten Bronze Nanocrystals. Reproduced from ref. 71 with permission from ACS, copyright 2013.

expected, the band gap is also increased with doping content. On the other hand, undoped CdO NCs whose LSPR was tuned from the wide range of NIR to the MIR region were synthesized *via* the decomposition of cadmium acetylacetonate ($Cd(acac)_2$) at 316 °C.[73] In order to promote oxygen deficiencies, reducing agents such bis(trimethylsilyl)amine (HMDS) were introduced into the reaction mixture. The idea behind using a reducing agent is to control the free electron concentration that will in turn affect the LSPR positioning. It has been found that by increasing the HMDS/Cd molar ratio, the NC diameter decreases monotonically from 44.9 to 5.2 nm. Fig. 25a shows the FTIR spectra of CdO NCs with different diameters. Evidently, as the diameter of the NCs decreases (increase in oxygen deficiency), the LSPR peak is shifted toward the NIR region. Furthermore, in Fig. 25b, the extinction coefficient of NCs dispersed in three different solvents, *i.e.* carbon tetrachloride (CCl_4), tetrachloroethylene (TCE), and carbon disulfide (CS_2), are shown. As expected, the LSPR peak was shifted to higher wavelength (redshift) as the refractive index of the solvent increased (see Fig. 25c).

Furthermore, fluorine, In co-doped CdO (FICO) NCs were synthesized *via* the heat-up method.[74] Fig. 26(a–c) show the

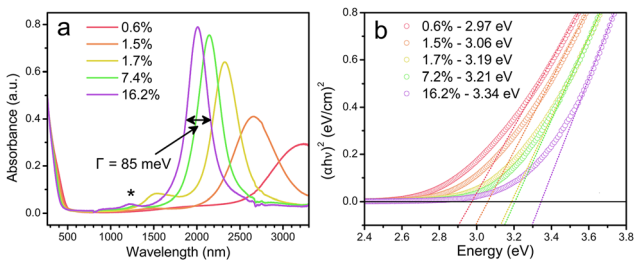

Fig. 24 (a) Solution-phase spectra of ICO nanocrystals dispersed in CCl_4 for five levels of % atomic doping of In. The fwhm or Γ is indicated for the 16.2% doped sample. (b) Plots of $(\alpha h\nu)^2$ *vs.* photon energy (eV) for five samples of spherical ICO nanocrystals. Open circles are measured data, dotted lines are linear fits, and the legend shows the extracted direct band-gap energies. Reproduced from ref. 71 with permission from ACS, copyright 2013.

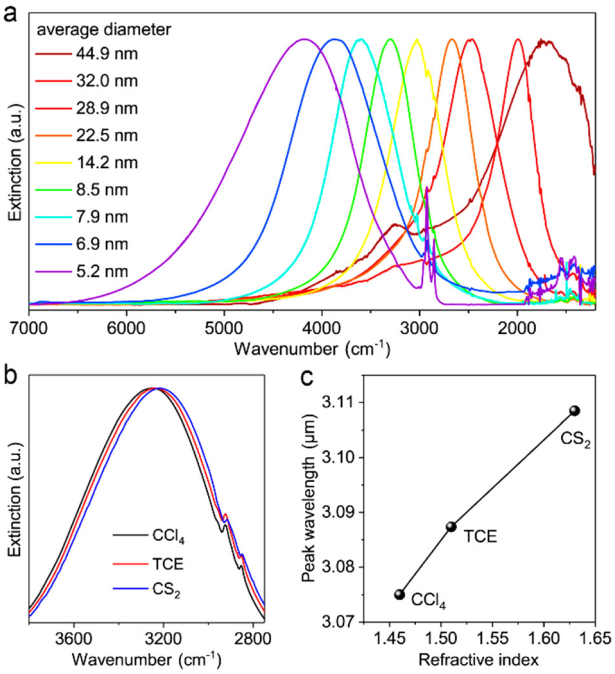

Fig. 25 (a) Normalized extinction spectra of size controlled CdO NCs synthesized with different HMDS/Cd ratios. (b) Extinction spectra of CdO NCs (8.5 ± 1.2 nm) dispersed in different solvents. (c) Plot of LSPR peak wavelength *versus* the refractive index of solvent. CCl_4: carbon tetrachloride, TCE: tetrachloroethylene, CS_2: carbon disulfide. Reproduced from ref. 73 with permission from ACS, copyright 2020.

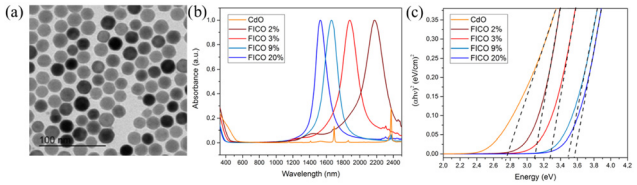

Fig. 26 (a) Transmission electron microscopy images of FICO 3% (diameter 20.2 ± 1.8 nm). (b) Normalized absorption spectra of FICO NC samples with different doping levels. (c) Plots of $(\alpha h\nu)^2$ *vs.* photon energy ($h\nu$) for the FICO NC samples shown in (b). Reproduced from ref. 74 with permission from ACS, copyright 2019.

TEM images, UV-vis-NIR spectra and Tauc plots of FICO NCs. As can be seen from Fig. 26a, the FICO NCs are found to be spherical in shape. At all the doping concentrations, sharp LSPR peaks were observed, which shifted to lower wavelength as the doping concentration increased (Fig. 26b). Furthermore, the band gap of FICO NCs also increased with an increase in the In doping level underlying the Burstein–Moss effect.

Future prospective applications: MOX NC based IR photodetector and PV self-powered chemical sensors

After a comprehensive review of the literature about the plasmonic properties of different MOX NCs, we come to their future prospective applications in optoelectronic devices. The first obvious applications of these materials are for IR photodetectors owing to the tuneable LSPR in the IR region. The continuous increase in interest in (IR) photodetectors has driven advances in imaging, satellite remote sensing, environmental monitoring, optical communications, security surveillance, gas identification, and biomedical engineering.[75,76] However, current commercial IR photodetectors developed using bulk compound semiconductors like InSb, Ge, HgCdTe, or InGaAs, still grapple with big issues such as high cost, toxicity, inflexibility, low environmental stability, complex fabrication processes, volume-dependent thermal noise, and limited pixel size.[75,77,78] Due to this, continuous efforts have been made to find alternative low-cost and highly efficient materials for IR photodetector applications. In this regard, 2D materials (graphene, MXene, TMDs, *etc.*)[22,75,79,80] and narrow-band-gap materials, such as PbS,[81] PbSe,[82] or InP,[83] were put forward. However, 2D materials still suffer from issues like (i) limited availability of 2D materials with a band gap, (ii) the lack of reproducibility in the fabrication process, (iii) poor stability in an ambient environment, (iv) slow/poor response dynamics, (v) poor selectivity and (vi) problems in large-scale production.[22,75,84–86] Additionally, the large-scale production of 2D materials is a common challenge faced by both applications.[22,75] On the other hand, IR photodetectors based on narrow-band-gap materials face several critical challenges, as discussed by Z. Wang *et al.*[76] in a comprehensive review article. In particular, the issues are the use of heavy toxic materials (*e.g.* Pb or Hg) and their better performance mainly in the NIR region,[81,87,88] while the development of MIR-based photodetectors remains a challenging task. Additionally, these QD-based IR photodetectors suffer from poor charge-carrier transport in QDs[76] which is a huge problem, as effective charge-carrier transport in photodetectors determines charge-carrier separation and collection.

Degenerately doped MOX NCs can be seen as IR detecting media because of the possibility of tuning the LSPR from the deep MIR to the NIR region by optimizing the carrier concentration using different dopants. Furthermore, the availability of scalable synthesis methods like heat-up or continuous growth makes it favourable over 2D materials. In an interesting piece of work, Qu *et al.*[89] explored the potential of ITO NCs for IR photodetector applications. Due to the weak photo-signal that is linked with the poor charge transport in NCs (a similar issue to narrow-band-gap QDs) and weak extraction of LSPR-assisted hot-electrons, very poor photodetector performance was observed. To overcome the obstacle of hot-electron extraction, a heterostructure of MOX NCs (ITO) and MoS_2 has recently been proposed, which we have already discussed in Section 3. However, when making optoelectronic devices like photodetectors, charge transport within the active material and their collection at the respective electrodes defines the efficiency of the devices. In this regard, the heterojunction between narrow-band-gap PbS QDs and ZnO nanowires (NWs) was proven to be effective,[81,87] in which the QDs act as an NIR sensitizer and NWs provide the conduction path to electrons. Indeed, the charge transport in NWs is believed to occur at a speed several

orders of magnitude faster than in nanoparticles like QDs or NCs, primarily attributed to the minimized scattering effects resulting from the limited presence of grain boundaries.[90] Additionally, due to the quantum confinement effect, NWs provide unidirectional and better control of charge transport, leading to high charge-carrier mobility.[90] Hence, the heterojunction of NCs with 2D materials, nanowires *etc.* can been seen as step forward to fabricate the future generation of IR photodetectors based on degenerately doped MOX NCs.

Furthermore, nanostructured MOXs have been explored and proven to be highly efficient for chemical sensing applications.[91–98] However, recently, the development of self-powered sensors for real-time environmental and health monitoring has gained momentum, driven by the urgency of the energy crisis, environmental pollution, and climate change.[23] Harnessing energy from sunlight is always an ideal and dependable choice due to its cleanliness, safety, and the vast energy reserves Earth receives from the sun. A sensor that harnesses energy from sunlight is known as a photovoltaic (PV) self-powered sensor.[79] However, the current state-of-the-art for PV self-powered sensors, whether utilizing sunlight or other activation sources, is still far from reaching the essential ''3S of a sensor'': sensitivity, selectivity, and stability.[22,23,99] In this regard, photoactivated (UV) MOX-based gas sensors have gained significant attention for developing RT or low-power-consuming sensors.[22] By fabricating these MOXs in different nanostructure forms and by tuning their band gap, photoactivation with visible light has also been achieved.[23] It was observed that by designing suitable device structures, these photoactivated MOX sensors are able to achieve self-sustaining operation using the photovoltaic (PV) effect.[100–102] To further extend light harvesting to the IR region, degenerately doped MOX NCs can be employed as an active sensing platform. Sturaro *et al.*[103] proposed gallium-doped zinc oxide (GZO) NC based optical (plasmonic) and chemiresistive sensors for the detection of hydrogen (H_2) and nitrogen dioxide (NO_2). To realize a sensing device, an NC thin film was deposited by spin-coating onto an SiO_2 substrate. The sensing measurements were performed at 80 and 200 °C. In the chemiresistive gas sensing of these NCs, the authors observed some response at room-temperature under illumination by blue light and the response increased with an increase in the operating temperature of the sensor. These were preliminary investigations, as many important factors, such as sensor selectivity, sensitivity and stability, need to be explored. However, it indeed gives us the idea and possibility to use degenerately doped MOX NCs to build PV self-powered sensors that harvest energy from UV-vis-IR radiation. In this sense, the heterostructure of NCs with MOX NWs can be effective. The reason behind this argument is that a chemiresistive sensor based on MOX NWs is already an established sensing platform and it showed fast response dynamics, selectivity, and stability due to the high surface-to-volume ratio, well-defined crystal orientation and controlled unidirectional electrical properties.[94,104,105]

Hence, by carefully manipulating the plasmonic properties of degenerately doped MOX NCs and using a suitable device configuration, a future generation of IR photodetectors and PV self-powered chemical sensors can be developed.

Conclusions

In conclusion, by reviewing the comprehensive literature, we have demonstrated the plasmonic properties of degenerately doped MOX NCs. Compared to the well-known hot injection method, continuous growth and heat-up represent large-scale production methods and were used significantly to produce various MOX NCs. Fabrication of 0D–2D heterostructures (ITO/MoS_2) for the extraction of LSPR-assisted hot-carriers is an interesting strategy. These types of strategies should also be utilized for other MOX NCs and ultrafast transient absorption studies need to be done to develop a deep understanding of plasmonic charge-carrier dynamics in MOX NCs. In fact, after reviewing the literature, we have realized that an advanced level of understanding in terms of synthesis, such as the growth mechanism of NCs, the incorporation of different dopants inside NCs and their effect on LSPR, and the roles of defects and tuning the LSPR over a wide range of the IR region by controlling NC size and doping content, have already been achieved. Now is the time to carry out studies at the device level, such as acquiring IV characteristics under illumination by IR light and understanding the mechanism of photogenerated charge carriers in different device configurations, such as heterojunctions, thin films of NCs, self-assembly *etc.* These types of studies are very important for the practical and prospective use of MOX NCs for a future generation of optoelectronic devices. Thus, we believe that degenerately doped MOX NCs have great potential for developing IR photodetectors, PV self-powered sensors and other potential optoelectronic devices, but an immense amount of dedicated work is required on a device level.

Author contributions

MS conceptualized and wrote the original draft of review. GMP conceptualized and edited the manuscript. FS edited the manuscript and arranged the funding.

Data availability

No primary research results, software or code have been included and no new data were generated or analysed as part of this review.

Conflicts of interest

There are no conflicts to declare.

Acknowledgements

This project has received funding from the European Research Council (ERC) under the European Union's Horizon 2020

research and innovation program (grant agreement no. [816313]) and under Horizon Europe (grant agreements no. [101061820]). GMP receives funding from the European Union (ERC, EOS, 101115925). Views and opinions expressed are, however, those of the author(s) only and do not necessarily reflect those of the European Union or the European Research Council. Neither the European Union nor the granting authority can be held responsible for them. This author also acknowledges financial support by the European Union's Next-GenerationEU Programme with the IPHOQS Infrastructure [IR0000016, ID D2B8D520, CUP B53C22001750006] ''Integrated Infrastructure Initiative in Photonic and Quantum Sciences''.

References

1 J. A. Faucheaux, A. L. D. Stanton and P. K. Jain, *J. Phys. Chem. Lett.*, 2014, **5**, 976–985.
2 A. Agrawal, S. H. Cho, O. Zandi, S. Ghosh, R. W. Johns and D. J. Milliron, *Chem. Rev.*, 2018, **118**, 3121–3207.
3 M. Yao, P. Shen, Y. Liu, B. Chen, W. Guo, S. Ruan and L. Shen, *ACS Appl. Mater. Interfaces*, 2016, **8**, 6183–6189.
4 F. Xu, H.-F. Lv, S.-Y. Wu and H.-P. Ho, *Sens. Actuators, B*, 2018, **259**, 709–716.
5 R. Bakhtiar, *J. Chem. Educ.*, 2013, **90**, 203–209.
6 X. Gu, T. Qiu, W. Zhang and P. K. Chu, *Nanoscale Res. Lett.*, 2011, **6**, 199.
7 L. Moscardi, G. M. Paternò, A. Chiasera, R. Sorrentino, F. Marangi, I. Kriegel, G. Lanzani and F. Scotognella, *J. Mater. Chem. C*, 2020, **8**, 13019–13024.
8 G. M. Paternò, C. Iseppon, A. D'Altri, C. Fasanotti, G. Merati, M. Randi, A. Desii, E. A. A. Pogna, D. Viola, G. Cerullo, F. Scotognella and I. Kriegel, *Sci. Rep.*, 2018, **8**, 3517.
9 R. Buonsanti, A. Llordes, S. Aloni, B. A. Helms and D. J. Milliron, *Nano Lett.*, 2011, **11**, 4706–4710.
10 S. D. Lounis, E. L. Runnerstrom, A. Llordés and D. J. Milliron, *J. Phys. Chem. Lett.*, 2014, **5**, 1564–1574.
11 J. M. Luther, P. K. Jain, T. Ewers and A. P. Alivisatos, *Nat. Mater.*, 2011, **10**, 361–366.
12 P. Yin, Y. Tan, H. Fang, M. Hegde and P. V. Radovanovic, *Nat. Nanotechnol.*, 2018, **13**, 463–467.
13 J. Q. Grim, L. Manna and I. Moreels, *Chem. Soc. Rev.*, 2015, **44**, 5897–5914.
14 X. Liu and M. T. Swihart, *Chem. Soc. Rev.*, 2014, **43**, 3908–3920.
15 K. Manthiram and A. P. Alivisatos, *J. Am. Chem. Soc.*, 2012, **134**, 3995–3998.
16 J. Shi, J. Zhang, L. Yang, M. Qu, D.-C. Qi and K. H. L. Zhang, *Adv. Mater.*, 2021, **33**, 2006230.
17 O. Bierwagen, *Semicond. Sci. Technol.*, 2015, **30**, 24001.
18 S. Wahyuningsih, I. Kartini, A. H. Ramelan, L. N. M. Z. Saputri and H. Munawaroh, *IOP Conf. Ser. Earth Environ. Sci.*, 2017, **75**, 12003.
19 M. Patel, H.-S. Kim and J. Kim, *Adv. Electron. Mater.*, 2015, **1**, 1500232.
20 Z. Ma, J. Zhang, H. Lyu, X. Ping, L. Pan and Y. Shi, in *Metal Oxides*, ed. S. Sagadevan, J. Podder and O.-B. M. A. Mohammad, Elsevier, 2022, pp. 117–150.
21 L. Li, C. X. Shan, B. H. Li, B. Yao, D. Z. Shen, B. Chu and Y. M. Lu, *J. Electron. Mater.*, 2010, **39**, 2467–2470.
22 R. Kumar, X. Liu, J. Zhang and M. Kumar, *Nano-Micro Lett.*, 2020, **12**, 164.
23 X.-L. Liu, Y. Zhao, W.-J. Wang, S.-X. Ma, X.-J. Ning, L. Zhao and J. Zhuang, *IEEE Sens. J.*, 2021, **21**, 5628–5644.
24 Q. Geng, Z. He, X. Chen, W. Dai and X. Wang, *Sens. Actuators, B*, 2013, **188**, 293–297.
25 J.-H. Lin, Y.-J. Chen, H.-Y. Lin and W.-F. Hsieh, *J. Appl. Phys.*, 2005, **97**, 33526.
26 D. C. Dai, S. J. Xu, S. L. Shi, M. H. Xie and C. M. Che, *Opt. Lett.*, 2005, **30**, 3377–3379.
27 J. E. Kuszynski, C. J. Fabiano, E. T. Nguyen, K. Mao, A. K. Ahuja, R. D. Schaller and G. F. Strouse, *J. Phys. Chem. C*, 2023, **127**, 22654–22661.
28 A. Devizis, V. Vaicikauskas and V. Gulbinas, *Appl. Opt.*, 2006, **45**, 2535–2539.
29 X. Zhang, C. Huang, M. Wang, P. Huang, X. He and Z. Wei, *Sci. Rep.*, 2018, **8**, 10499.
30 C. Trovatello, F. Katsch, N. J. Borys, M. Selig, K. Yao, R. Borrego-Varillas, F. Scotognella, I. Kriegel, A. Yan, A. Zettl, P. J. Schuck, A. Knorr, G. Cerullo and S. D. Conte, *Nat. Commun.*, 2020, **11**, 5277.
31 G. Grancini, M. Maiuri, D. Fazzi, A. Petrozza, H.-J. Egelhaaf, D. Brida, G. Cerullo and G. Lanzani, *Nat. Mater.*, 2013, **12**, 29–33.
32 M. Maiuri, M. Garavelli and G. Cerullo, *J. Am. Chem. Soc.*, 2020, **142**, 3–15.
33 N. Kinsey, C. DeVault, J. Kim, M. Ferrera, V. M. Shalaev and A. Boltasseva, *Optica*, 2015, **2**, 616–622.
34 G. X. Ni, L. Wang, M. D. Goldflam, M. Wagner, Z. Fei, A. S. McLeod, M. K. Liu, F. Keilmann, B. Özyilmaz, A. H. Castro Neto, J. Hone, M. M. Fogler and D. N. Basov, *Nat. Photonics*, 2016, **10**, 244–247.
35 P. Guo, R. D. Schaller, J. B. Ketterson and R. P. H. Chang, *Nat. Photonics*, 2016, **10**, 267–273.
36 I. Kriegel, C. Urso, D. Viola, L. De Trizio, F. Scotognella, G. Cerullo and L. Manna, *J. Phys. Chem. Lett.*, 2016, **7**, 3873–3881.
37 Q. Guo, Z. Qin, Z. Wang, Y.-X. Weng, X. Liu, G. Xie and J. Qiu, *ACS Nano*, 2018, **12**, 12770–12777.
38 C. Lee, Y. Park and J. Y. Park, *RSC Adv.*, 2019, **9**, 18371–18376.
39 M. Guizzardi, M. Ghini, A. Villa, L. Rebecchi, Q. Li, G. Mancini, F. Marangi, A. M. Ross, X. Zhu, I. Kriegel and F. Scotognella, *J. Phys. Chem. Lett.*, 2022, **13**, 9903–9909.
40 V. K. LaMer and R. H. Dinegar, *J. Am. Chem. Soc.*, 1950, **72**, 4847–4854.
41 C. B. Murray, D. J. Norris and M. G. Bawendi, *J. Am. Chem. Soc.*, 1993, **115**, 8706–8715.
42 S. Ghosh, M. Saha and S. K. De, *Nanoscale*, 2014, **6**, 7039–7051.

43 T. Hyeon, S. S. Lee, J. Park, Y. Chung and H. B. Na, *J. Am. Chem. Soc.*, 2001, **123**, 12798–12801.
44 B. H. Kim, W. Ko, J. H. Kim, J. S. Georgiou, M. S. Bootharaju, J. Park and T. Hyeon, *Isr. J. Chem.*, 2023, e202200103.
45 A. W. Jansons, K. M. Koskela, B. M. Crockett and J. E. Hutchison, *Chem. Mater.*, 2017, **29**, 8167–8176.
46 B. M. Crockett, A. W. Jansons, K. M. Koskela, D. W. Johnson and J. E. Hutchison, *ACS Nano*, 2017, **11**, 7719–7728.
47 M. Xi and B. M. Reinhard, *J. Phys. Chem. C*, 2018, **122**, 5698–5704.
48 A. M. Schimpf, S. D. Lounis, E. L. Runnerstrom, D. J. Milliron and D. R. Gamelin, *J. Am. Chem. Soc.*, 2015, **137**, 518–524.
49 M. A. Blemker, S. L. Gibbs, E. K. Raulerson, D. J. Milliron and S. T. Roberts, *ACS Photonics*, 2020, **7**, 1188–1196.
50 E. L. Runnerstrom, A. Bergerud, A. Agrawal, R. W. Johns, C. J. Dahlman, A. Singh, S. M. Selbach and D. J. Milliron, *Nano Lett.*, 2016, **16**, 3390–3398.
51 S. D. Lounis, E. L. Runnerstrom, A. Bergerud, D. Nordlund and D. J. Milliron, *J. Am. Chem. Soc.*, 2014, **136**, 7110–7116.
52 B. Tandon, S. Ghosh and D. J. Milliron, *Chem. Mater.*, 2019, **31**, 7752–7760.
53 Y. Gu, Z. Zhu, J. Song and H. Zeng, *Nanoscale*, 2017, **9**, 19374–19383.
54 S. H. Cho, K. M. Roccapriore, C. K. Dass, S. Ghosh, J. Choi, J. Noh, L. C. Reimnitz, S. Heo, K. Kim, K. Xie, B. A. Korgel, X. Li, J. R. Hendrickson, J. A. Hachtel and D. J. Milliron, *J. Chem. Phys.*, 2020, **152**, 14709.
55 P. Yin, Y. Tan, M. J. Ward, M. Hegde and P. V. Radovanovic, *J. Phys. Chem. C*, 2019, **123**, 29829–29837.
56 H. Fang, M. Hegde, P. Yin and P. V. Radovanovic, *Chem. Mater.*, 2017, **29**, 4970–4979.
57 P. Wainer, O. Kendall, A. Lamb, S. J. Barrow, A. Tricoli, D. E. Gómez, J. van Embden and E. Della Gaspera, *Chem. Mater.*, 2019, **31**, 9604–9613.
58 S. Fiedler, L. O. L. C. Lem, C. Ton-That, M. Schleuning, A. Hoffmann and M. R. Phillips, *Sci. Rep.*, 2020, **10**, 2553.
59 M. Singh and F. Scotognella, *Micromachines*, 2023, **14**, mi14030536.
60 E. Della Gaspera, A. S. R. Chesman, J. van Embden and J. J. Jasieniak, *ACS Nano*, 2014, **8**, 9154–9163.
61 M. Saha, S. Ghosh, V. D. Ashok and S. K. De, *Phys. Chem. Chem. Phys.*, 2015, **17**, 16067–16079.
62 E. Della Gaspera, N. W. Duffy, J. van Embden, L. Waddington, L. Bourgeois, J. J. Jasieniak and A. S. R. Chesman, *Chem. Commun.*, 2015, **51**, 12369–12372.
63 W. Zhu, T. Kammuri, S. Kitamura, M. Sturaro, A. Martucci and G. Pezzotti, *J. Phys. D: Appl. Phys.*, 2018, **51**, 85302.
64 J. T. Lee, S. Hati, M. M. Fahey, J. M. Zaleski and R. Sardar, *Chem. Mater.*, 2022, **34**, 3053–3066.
65 Y.-Y. Li, C.-Y. Zhong, M.-X. Li, Q.-Y. Zhang, Y. Chen, Z.-Q. Liu and J. Z. Zhang, *J. Mater. Chem. C*, 2021, **9**, 1614–1621.
66 J. Chen, Y. Ren, T. Hu, T. Xu and Q. Xu, *Appl. Surf. Sci.*, 2019, **465**, 517–525.
67 T. Masuda and H. Yao, *J. Phys. Chem. C*, 2020, **124**, 15460–15467.
68 P. Li, L. Zhu, C. Ma, L. Zhang, L. Guo, Y. Liu, H. Ma and B. Zhao, *ACS Appl. Mater. Interfaces*, 2020, **12**, 19153–19160.
69 T. M. Mattox, A. Bergerud, A. Agrawal and D. J. Milliron, *Chem. Mater.*, 2014, **26**, 1779–1784.
70 O. A. Balitskii, D. Moszyński and Z. Abbas, *RSC Adv.*, 2016, **6**, 59050–59054.
71 T. R. Gordon, T. Paik, D. R. Klein, G. V. Naik, H. Caglayan, A. Boltasseva and C. B. Murray, *Nano Lett.*, 2013, **13**, 2857–2863.
72 S. Ghosh, M. Saha, S. Paul and S. K. De, *Small*, 2017, **13**, 1602469.
73 Z. Liu, Y. Zhong, I. Shafei, S. Jeong, L. Wang, H. T. Nguyen, C.-J. Sun, T. Li, J. Chen, L. Chen, Y. Losovyj, X. Gao, W. Ma and X. Ye, *Nano Lett.*, 2020, **20**, 2821–2828.
74 R. Giannuzzi, F. De Donato, L. De Trizio, A. G. Monteduro, G. Maruccio, R. Scarfiello, A. Qualtieri and L. Manna, *ACS Appl. Mater. Interfaces*, 2019, **11**, 39921–39929.
75 J. Zha, M. Luo, M. Ye, T. Ahmed, X. Yu, D.-H. Lien, Q. He, D. Lei, J. C. Ho, J. Bullock, K. B. Crozier and C. Tan, *Adv. Funct. Mater.*, 2022, **32**, 2111970.
76 Z. Wang, Y. Gu, X. Li, Y. Liu, F. Liu and W. Wu, *Adv. Opt. Mater.*, 2023, **11**, 2300970.
77 M. Long, Y. Wang, P. Wang, X. Zhou, H. Xia, C. Luo, S. Huang, G. Zhang, H. Yan, Z. Fan, X. Wu, X. Chen, W. Lu and W. Hu, *ACS Nano*, 2019, **13**, 2511–2519.
78 L. Ye, H. Li, Z. Chen and J. Xu, *ACS Photonics*, 2016, **3**, 692–699.
79 Y. Niu, J. Zeng, X. Liu, J. Li, Q. Wang, H. Li, N. F. de Rooij, Y. Wang and G. Zhou, *Adv. Sci.*, 2021, **8**, 2100472.
80 S. Gasso and A. Mahajan, *ACS Appl. Nano Mater.*, 2023, **6**, 6678–6692.
81 H. Zhong, L. Tang, P. Tian, L. Yu, W. Zuo and K. S. Teng, *Sensors*, 2023, **23**, s23042254.
82 Y. Shi, Z. Wu, X. Dong, P. Chen, J. Wang, J. Yang, Z. Xiang, M. Shen, Y. Zhuang, J. Gou, J. Wang and Y. Jiang, *Nanoscale*, 2021, **13**, 12306–12313.
83 G. Almeida, R. F. Ubbink, M. Stam, I. du Fossé and A. J. Houtepen, *Nat. Rev. Mater.*, 2023, **8**, 742–758.
84 M. Malik, M. A. Iqbal, J. R. Choi and P. V. Pham, *Front. Chem.*, 2022, **10**, 905404.
85 K. Zhang, L. Zhang, L. Han, L. Wang, Z. Chen, H. Xing and X. Chen, *Nano Express*, 2021, **2**, 12001.
86 E. Lee and H. Yoo, *Molecules*, 2021, **26**, 5056.
87 H. Wang, T. Kubo, J. Nakazaki, T. Kinoshita and H. Segawa, *J. Phys. Chem. Lett.*, 2013, **4**, 2455–2460.
88 J. Wang and J. Chen, *Surf. Interfaces*, 2022, **30**, 101945.
89 J. Qu, C. Livache, B. Martinez, C. Gréboval, A. Chu, E. Meriggio, J. Ramade, H. Cruguel, X. Z. Xu, A. Proust, F. Volatron, G. Cabailh, N. Goubet and E. Lhuillier, *ACS Appl. Nano Mater.*, 2019, **2**, 1621–1630.
90 F. Mei, D. Sun, S. Mei, J. Feng, Y. Zhou, J. Xu and X. Xiao, *Adv. Phys. X*, 2019, **4**, 1592709.
91 M. Singh, N. Kaur, A. Casotto, L. Sangaletti, N. Poli and E. Comini, *J. Mater. Chem. A*, 2022, **10**, 3178–3189.

92 M. Singh, N. Kaur, A. Casotto, L. Sangaletti and E. Comini, *Sens. Actuators, B*, 2023, **384**, 133653.
93 N. Kaur, M. Singh and E. Comini, *Adv. Mater. Interfaces*, 2021, 2101629.
94 N. Kaur, M. Singh and E. Comini, *Langmuir*, 2020, **36**, 6326–6344.
95 N. Kaur, D. Zappa, V.-A. Maraloiu and E. Comini, *Adv. Funct. Mater.*, 2021, 2104416.
96 M. H. Raza, N. Kaur, E. Comini and N. Pinna, *Adv. Mater. Interfaces*, 2021, **8**, 2100939.
97 N. Kaur, M. Singh, A. Moumen, G. Duina and E. Comini, *Materials*, 2020, **13**, ma13132974.
98 D. Zappa, V. Galstyan, N. Kaur, H. M. M. Munasinghe Arachchige, O. Sisman and E. Comini, *Anal. Chim. Acta*, 2018, 1–23.
99 J. Zhu, H. Wen, Y. Fan, X. Yang, H. Zhang, W. Wu, Y. Zhou and H. Hu, *Microchem. J.*, 2022, **181**, 107833.
100 M. W. G. Hoffmann, L. Mayrhofer, O. Casals, L. Caccamo, F. Hernandez-Ramirez, G. Lilienkamp, W. Daum, M. Moseler, A. Waag, H. Shen and J. D. Prades, *Adv. Mater.*, 2014, **26**, 8017–8022.
101 J.-L. Hou, C.-H. Wu and T.-J. Hsueh, *Sens. Actuators, B*, 2014, **197**, 137–141.
102 R. Tanuma and M. Sugiyama, *Phys. Status Solidi*, 2019, **216**, 1800749.
103 M. Sturaro, E. Della Gaspera, N. Michieli, C. Cantalini, S. M. Emamjomeh, M. Guglielmi and A. Martucci, *ACS Appl. Mater. Interfaces*, 2016, **8**, 30440–30448.
104 N. Kaur, M. Singh, A. Casotto, L. Sangaletti and E. Comini, *Chem. Commun.*, 2023, **59**, 1329–1332.
105 M. Singh, N. Kaur, G. Drera, A. Casotto, L. S. Ermenegildo and E. Comini, *Adv. Funct. Mater.*, 2020, **30**, 2003217.